Structure and dielectric properties of MgO-coated BaTiO$_3$ ceramics

Xin Lai[1] · Hua Hao[1,3] · Zhen Liu[2] · Shangshu Li[2] · Yiren Liu[2] · Marwa Emmanuel[1] · Zhonghua Yao[1,3] · Minghe Cao[1] · Dawei Wang[4] · Hanxing Liu[2]

Abstract

BaTiO$_3$@xMgO (BT@xMg, $x = 0$–7 mol%) ceramics were prepared by MgO-coated BT powders, which were synthesized by a chemical precipitation method. The effects of MgO coating on the phase structure, microstructure and dielectric properties of BT@xMg ceramics were explored. The solid solubility of Mg^{2+} at B-site in BT was about 0.8 mol%, which was confirmed by the c/a ratio variation. When $x < 0.8$ mol%, the degree of tetragonality and Curie temperature were decreased with the increase of MgO content, and it can be attributed to the B-site substitution of Mg^{2+} ion. At the same time, the decrease in grain size lead to the appearance of Orthorhombic at room temperature. With excess MgO beyond the solid solution limitation (≥ 0.8 mol%), inhomogeneous distribution of Mg was observed around grain boundaries which resulted in a core–shell structure in ceramics. The dielectric temperature stability was effectively improved with a low dielectric loss of ~0.01. Furthermore, a weak dependence of dielectric properties on MgO content was observed, where the composites of BT@3 Mg and BT@5 Mg ceramics met X8R standard.

1 Introduction

Multilayer ceramic capacitors (MLCCs) are the most widely used basic components in electronics. BaTiO$_3$ (BT) has been commercially chosen as the dielectric ceramics for MLCCs, due to its environmental friendliness and excellent dielectric properties [1, 2]. However, the dielectric constant (ε_r) of pure BT ceramics has a sharp dielectric peak around Curie temperature (T_c), which exhibits a poor temperature stability. Therefore, it is difficult for BT to satisfy the X8R specification, where a maximum capacitance variation of $\pm 15\%$ is required over a temperature range of -55 °C to $+150$ °C.

✉ Hua Hao
haohua@whut.edu.cn

1   State Key Laboratory of Silicate Materials for Architectures, School of Material Science and Engineering, Wuhan University of Technology, Wuhan 430070, China

2   State Key Laboratory of Advanced Technology for Materials Synthesis and Processing, International School of Material Science and Engineering, Wuhan University of Technology, Wuhan 430070, China

3   Foshan Xianhu Laboratory of the Advanced Energy Science and Technology Guangdong Laboratory, Xianhu Hydrogen Valley, Foshan 528200, China

4   Department of Materials Science and Engineering, University of Sheffield, Sheffield S1 3JD, UK

It is well-known that this issue can be effectively solved by element doping in BT ceramics [3, 4], such as La, Ho, Dy, Y, Mg, Ca, Mn, Al, etc. [5–12]. Among these dopants, MgO additive was reported to effectively improve the dielectric temperature stability of BT-based ceramics in an ultra-broad temperature range by inhibiting elements diffusion and forming a core–shell structure [13–15]. Mg^{2+} ion was also reported to substitute B-site ion and lead to the change of lattice constant, which was attributed to the close ionic radius between Mg^{2+} ion (0.605 Å) and Ti^{4+} ion (0.720 Å) [16].

At the same time, different preparation methods were reported to significantly affect the substitution behavior of Mg^{2+} ion in BT [17]. Uniform coating layer and inhomogeneous "core–shell" structure was obtained by chemical precipitation method, compared to the traditional solid-state method [2, 18]. Moreover, materials transport would be significantly retarded by a uniform coating layer of MgO as well as deactivating the sintering kinetics [16]. It results in element gradient distribution to form a core–shell structure, which effectively improved the dielectric properties and reliability of BT-based ceramics co-doped with rare earth elements [19].

In this work, MgO-coated BT (BT@xMg) powders were prepared by chemical precipitation method to obtain a core–shell structure, and then the phase structure,

microstructure, and dielectric properties of BT@xMg ceramics were studied in detail.

2 Experimental

Commercial BT powder (99.9%, grain size 200 nm, Shandong Sinocera Functional Material) was coated by a homogeneous precipitation method and dispersed in distilled water with a few drops of acetic acid mixed to obtain a suspension. Then the suspension was bathed in water at 40 °C for 30 min and subjected to ultrasonic dispersion for 30 min to obtain evenly dispersed suspension. $Mg(CH_3COO)_2 \cdot 4H_2O$ (99%) as magnesium source was stirred and dissolved in deionized water to create a magnesium solution. Afterwards, magnesium solution was added and mixed into BT suspension according to the stoichiometric composition BT@xMg, where $x=0$–7 mol% of BT. Then, ammonia was added into the suspension to adjust the pH value to ~ 10, thus resulting in magnesium ion precipitation on BT particles. At last, the BT suspension precipitated with magnesium ion was water bathed at 40 °C for 24 h and then calcined at 700 °C for 2 h to obtain the MgO-coated BT powder, BT@xMg. For comparison, MgO was also produced by chemical precipitation method Mg(p). Then, 5 wt% polyvinyl alcohol (PVA) binder was added to the BT@xMg ($x=0$–7 mol%) powders, followed by pressing the pellets. PVA was burned off through heating the pellets at 600 °C for 2 h and subsequently the green pellets were sintered at 1250–1325 °C for 2 h. In order to test the electrical properties, the Ag electrode was fired on both sides of the polished samples at 600 °C for 1 h.

The microstructure of sintered samples was investigated by a field emission scanning electron microscope (FE-SEM, Zeiss Ultra Plus, Zeiss, Germany) operated at 20 kV and a transmission electron microscopy (TEM, Talos F200S) operated at 200 kV. An energy-dispersive spectroscopy (EDS) was equipped on TEM to identify chemical elements. An X-ray powder diffractometer (XRD, PANalytical X'Pert PRO, the Netherlands), with Cu Kα ~ 1.54056 Å as X-ray source and a scanning speed of 2°/min, was used to identify the crystal phase. The XRD data were then refined by using a GSAS software. A Stokes-shifted Raman microscope (InVia, RENISHAW) using a 633 nm He–Ne laser was employed to examine the local structure from 100 to 1000 cm^{-1} at room temperature. Dielectric properties were measured by a LCR meter (HP 4284A, Agilent) in a temperature range from − 60 to 200 °C.

3 Results and discussion

The XRD spectra of Mg(p) powder are shown in Fig. 1, which confirmed that pure MgO phase was produced by the precipitate method.

The XRD spectra of BT@xMg ($x=0$–7 mol%) ceramic powders are shown in Fig. 2a. The phase structures of all samples were typical perovskite structure. An additional enlarged diffraction peak was observed around 33° (Fig. 2d) which was related to the second phase and would be further explored by the EDS analysis. In addition, the enlarged spectra in 2θ of 44°–45° are given in Fig. 2b. The diffraction peaks at 2θ ~ 45° gradually changed from splitting peaks to a single one which indicated a structure transition from tetragonal to cubic phase for BT@xMg ceramics with x increasing ($x \leq 0.8$ mol%). The XRD patterns were further refined by Rietveld refinement using GSAS. The lattice constants a, c were calculated and the c/a value of BT@xMg ceramic as a function of MgO content are plotted in Fig. 2c. It was observed that the c/a value decreased as x increasing up to 0.8% which indicating the decrease in tetragonality. However, the c/a value became stable with further increasing x. The c/a value consistently was higher than 1 which indicated that a tetragonal phase existed in all the samples. Moreover, the stable value of c/a confirmed that the solid solubility of Mg^{2+} at BT was about 0.8 mol%, which was close to the reported value of ~ 1 mol% [20, 21].

According to previous studies, there were commonly two explanations for the decrease in tetragonality. It was usually considered that Mg^{2+} ion replaced Ti^{4+} ion as acceptor dopant and generated oxygen vacancies, as shown in Eq. 1, resulting in the reduction of tetragonality in BT@xMg ceramics [22, 23].

$$BaO + MgO \rightarrow Ba_{Ba} + Mg''_{Ti} + 2O_O + V_O^{\cdot\cdot} \qquad (1)$$
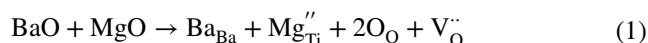
Another explanation was the change in the tolerance factor (t) which is obtained through the ionic radius model [24]. Tolerance factor, t, was calculated by Eq. 2. It was obvious
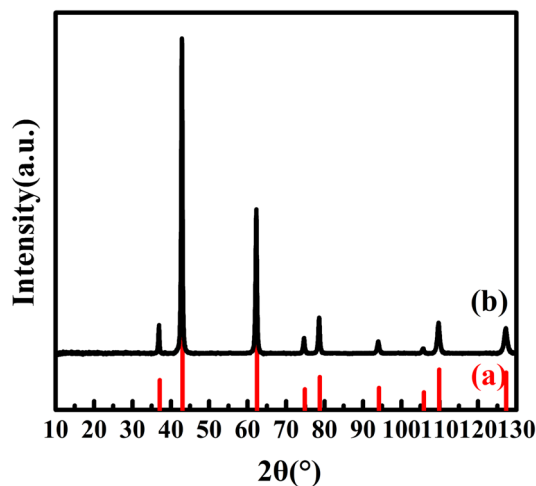

Fig. 1 XRD pattern of Mg(p) powder prepared by precipitation method (b) and MgO standard pattern (a)
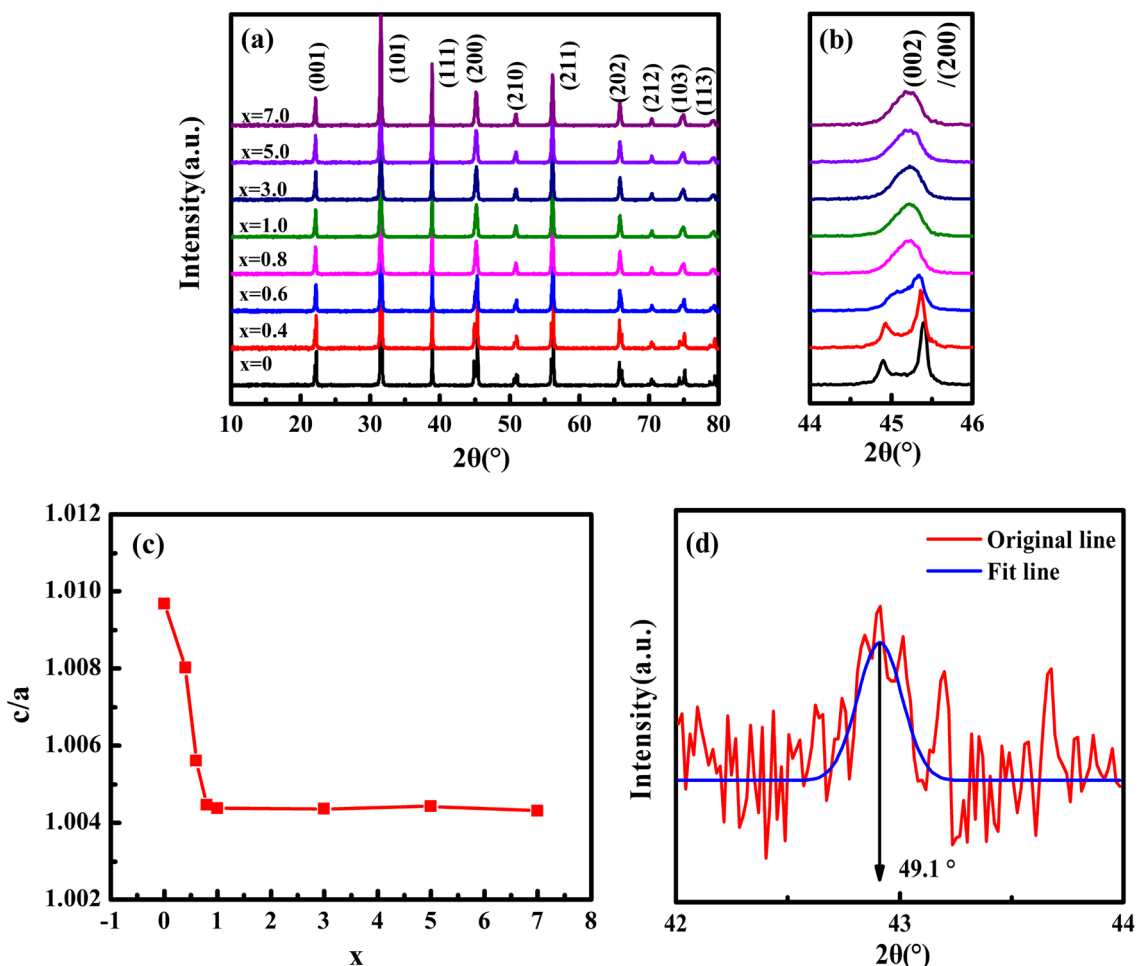
Fig. 2 XRD patterns of BT@xMg (x = 0–7 mol%) ceramics powder (**a**), enlarged from 44.0° to 46.0° (**b**), and c/a values as a function of x (**c**), and the diffraction peak of second phase (**d**)

that insolvent dopants with smaller ion radius in Ba-site or lager ion radius in Ti site reduced t of BT to 1 and stabilized the cubic phase in a lower temperature which led to the reduction of tetragonality and Tc [9].

$$t = \frac{R_A + R_O}{\sqrt{2}(R_B + R_O)} \qquad (2)$$

Raman spectroscopy was reported to detect the site occupancy of dopants in BT [25]. The vibration peak at 800 cm^{-1} is the A_{1g} breathing mode of TiO$_6$ octahedron, which is Raman inactive in pure BT due to the symmetrical mode without polarization change. However, it will become Raman active when there are multiple B-site species including titanium vacancies in BT [26]. Also the vibration intensity is affected by the concentration of B-site species. Raman spectra of BT@xMg (x = 0–7 mol%) ceramics are given in Fig. 3. The broad vibration peaks at 263, 521, 719 cm^{-1} and a sharp vibration peak at 311 cm^{-1} proved the tetragonal

phase structure of BT@xMg ceramics [20]. Moreover, the vibration intensity in 311 cm^{-1} decreased slightly with increasing x, which indicated the tetragonality was reduced, being consistent with the XRD results (Fig. 2). At the same time, no vibration peak was found around 800 cm^{-1} indicating Raman inactive mode was still by Mg^{2+} ion substituting Ti site [16, 22], which was mainly attributed to the low solid solubility of Mg^{2+} ion at Ti site (0.8 mol%) below the Raman detectable limitation, compared to other reported values > 1 mol% [25]. Furthermore, a new Raman mode at 192 cm^{-1} was observed when $x \geq 0.8$ mol%, which was the characteristic of orthorhombic BT [27]. It is indicated that the orthorhombic phase appeared at room temperature in BT@xMg ceramics and the orthorhombic-tetragonal transition temperature (T_1) of BT@xMg ceramics was higher than room temperature when $x \geq 0.8$ mol%. It has been reported that the orthorhombic phase could more efficiently reduce transformation stresses and make itself more stable compared to tetragonal phase. As a result, orthorhombic phase
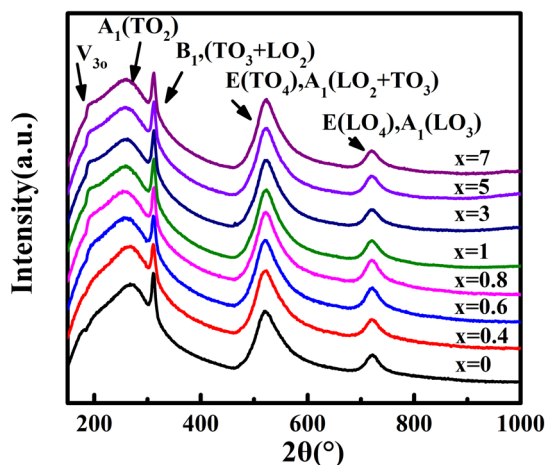
Fig. 3 Raman spectrums of BT@xMg ($x = 0$–7 mol%) ceramics

would become more stable at room temperature when the grain size is reduced [28]. The reduced grain size was in agreement to SEM results latter.

The SEM images of BT@xMg ceramics are shown in Fig. 4. The average grain size of pure BT ceramic was about ~100 μm and then significantly decreased to ~200 nm with the increase of MgO content. However, the grain size was almost unchanged when $x \geq 0.8$ mol%. BT@xMg ceramic samples with $x = 0.6$ and $x = 5$ mol% were chosen to be examined by TEM (Fig. 5), in which $x = 0.6$ mol% is within the solid solution limitation and $x = 5$ mol% is exceeded. Figure 5a$_1$ and b$_1$ show bright-field transmission electron image and the corresponding selected area electron diffraction (SAED) pattern collected along the [001] zone axes of each sample indicated a single-crystalline tetragonal structure for both samples as shown in the inset of Fig. 5a$_1$ and b$_1$, in agreement to the XRD and Raman data (Figs. 2 and 3). The homogenous distribution of Mg element was observed in sample of $x = 0.6$ mol% (Fig. 5a$_2$), whereas higher Mg content was found at the grain boundaries than that in the grains (Fig. 5b$_3$, b$_4$) when $x = 5$ mol%. It was thus confirmed that MgO tended to stay at the grain boundaries when Mg content was higher than the limitation of solid solubility, where a thin layer with uneven Mg element distribution could be formed near the grain boundaries. Park et al. [16] has reported similar phenomenon that excess MgO would aggregate at grain boundaries inhibiting ion diffusion when sintered. Moreover, the secondary phase enriched with Mg was found in BT@5 Mg ceramics, as shown in Fig. 5b$_2$.

The temperature dependence of dielectric constant and loss at 1–1000 kHz of BT@xMg ceramic is shown in Fig. 6. A clear double dielectric peaks were observed in the dielectric temperature curve when $x < 0.8$ mol%, corresponding to phase transition temperatures of orthorhombic to tetragonal (T_1) and tetragonal to cubic (T_c), respectively.

T_c of BT@xMg ceramics was decreased with the increase of MgO content as shown in Fig. 7. And then T_c became stable at $x = 0.8$ mol%, associated to the variation of c/a ratio as shown in Fig. 2(c).

Based on previous studies [10], defects including O vacancies and Ti site vacancies can drastically reduce T_c of BT-based ceramic by destructing the TiO$_6$ octahedron in lattice, which suppressed the cooperative interactions required to induce ferroelectricity in BT. In this work, the shifting effect of Mg^{2+} was more than 25 °C/at.% when $x < 0.8$ mol%, which was due to the generation of O vacancies by Mg^{2+} substituting in Ti site. In addition, the dielectric loss of BT@xMg ($x < 0.8$) ceramics slightly increased above T_c compared to pure BT ceramics as shown in Fig. 7, which was a result of increasing leakage conductivity at higher temperatures [29].

There were three dielectric peaks observed in the dielectric curve for BT@xMg ($x \geq 0.8$ mol%) ceramics as shown in Fig. 6. Two dielectric peaks near T_c may be related to the core–shell structure of BT@xMg ceramics. One peak stays at 130 °C ascribed to the BT core, and another peak around 110 °C was considered to be related to the shell phase with MgO addition. This phenomenon could be explained by the existence of core–shell structure confirmed by TEM analysis (Fig. 5b$_4$), which make the dielectric performance more stable [30]. In addition, the dielectric curve showed a weak dependence to MgO content, which was mainly due to the content of Mg^{2+} ion that exceeded the solution limitation when $x \geq 0.8$ mol% [16].

On the other hand, T_1 of pure BT here is 19.25 °C. And then increased to ~30 °C for BT@xMg ($x \geq 0.8$ mol%) ceramics, which further confirmed the presence of orthorhombic phase at room temperature, being consistent with Raman results (Fig. 3). In addition, the dielectric loss dramatically decreased when $x \geq 0.8$ mol%, as shown in Table 1, which should be attributed to the formation of "buffer layer" by excess MgO at grain boundaries effectively reducing the interface polarization [31]. Finally, a good dielectric temperature stability was achieved when $x = 3$, 5 mol%, satisfying the X8R specification (Table 1), which can be used as a base material to further improve the temperature stability of dielectric materials.

4 Conclusion

In summary, BT powders were coated with different MgO contents by the chemical precipitation method, and the phase structure, microstructure, and dielectric properties of BT@xMg ceramics were investigated. The lattice teragonality of ceramics was decreased with increasing MgO content but still retained tetragonal phase. The T_c shifted to low temperature with a rate of > 25 °C/at.%, indicating

Fig. 4 SEM images of the BT@xMg (x=0–7 mol%) ceramics **a** x=0, **b** x=0.4, **c** x=0.6, **d** x=0.8, **e** x=1, **f** x=3, **g** x=5, **h** x=7
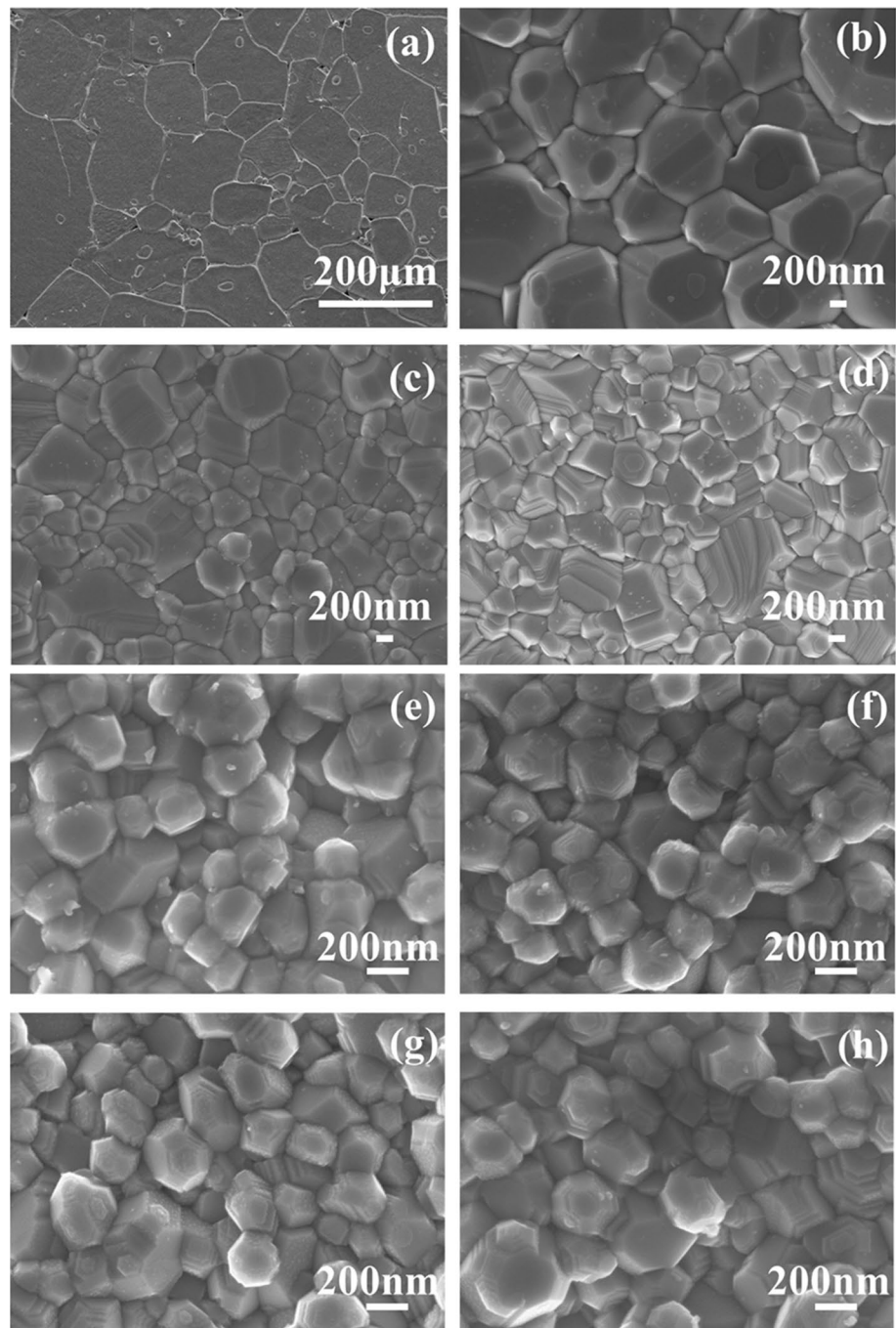
Mg^{2+} ion substitute in Ti site. In addition, it was found that the solid solution limitation of Mg^{2+} ion substituting Ti^{4+} ion was ~ 0.8 mol%. When $x \geq 0.8$ mol%, Mg^{2+} ions were found to stay at grain boundaries and produced the secondary phase. The core–shell structure was obtained by Mg gradient distribution and resulted in stable dielectric properties. The BT@xMg ceramics with x = 3, 5 mol% exhibited good temperature stability of ± 15% in between − 50 °C and 150 °C, meeting the standard X8R.

Fig. 5 Bright-field transmission electron image (a_1, b_1) and selected area electron diffraction (SAED) image viewed along [001] zone axis, HAADF transmission electron image (a_2, b_2, b_3), and Mg element distribution image, respectively, of BT@0.6 Mg and BT@5 Mg ceramics, EDS line profiles of Mg element (b_4) along the straight lines from point A to point B for BT@5 Mg ceramics
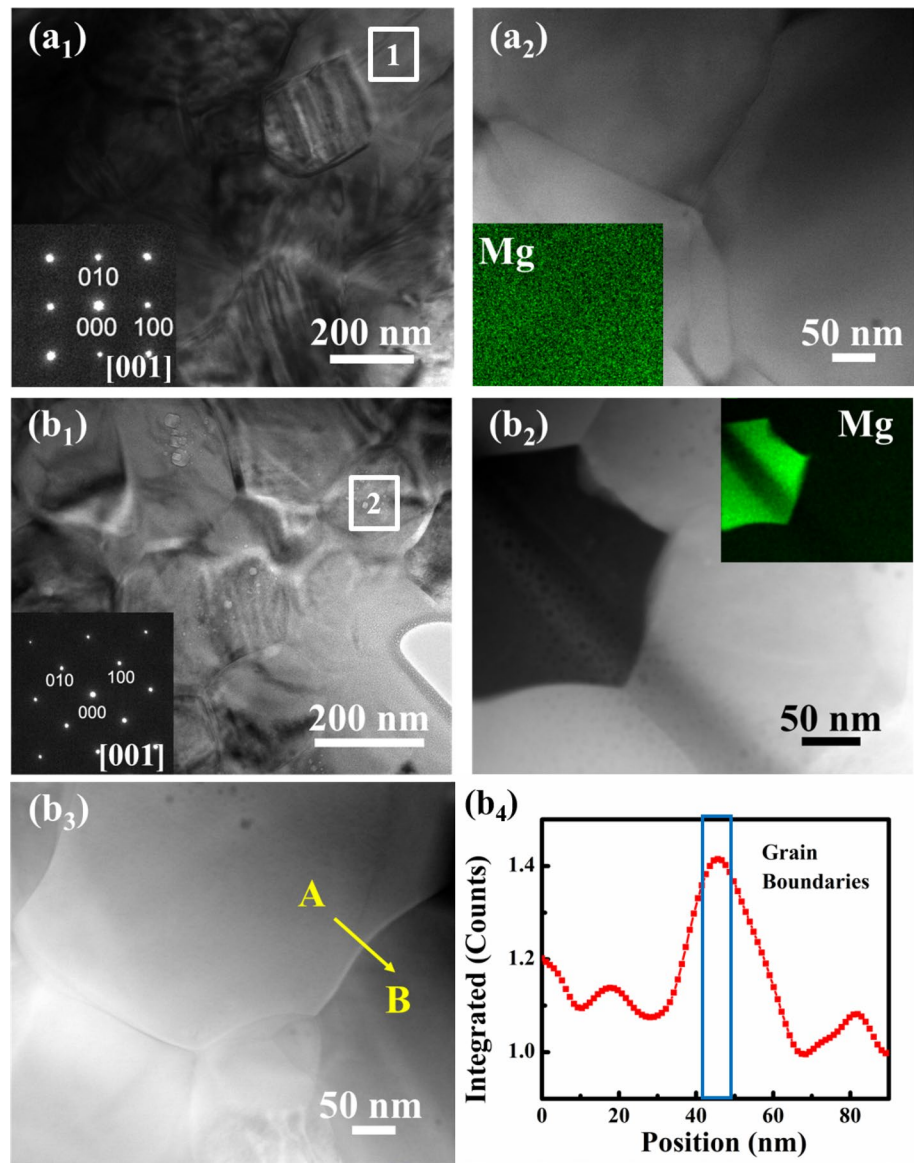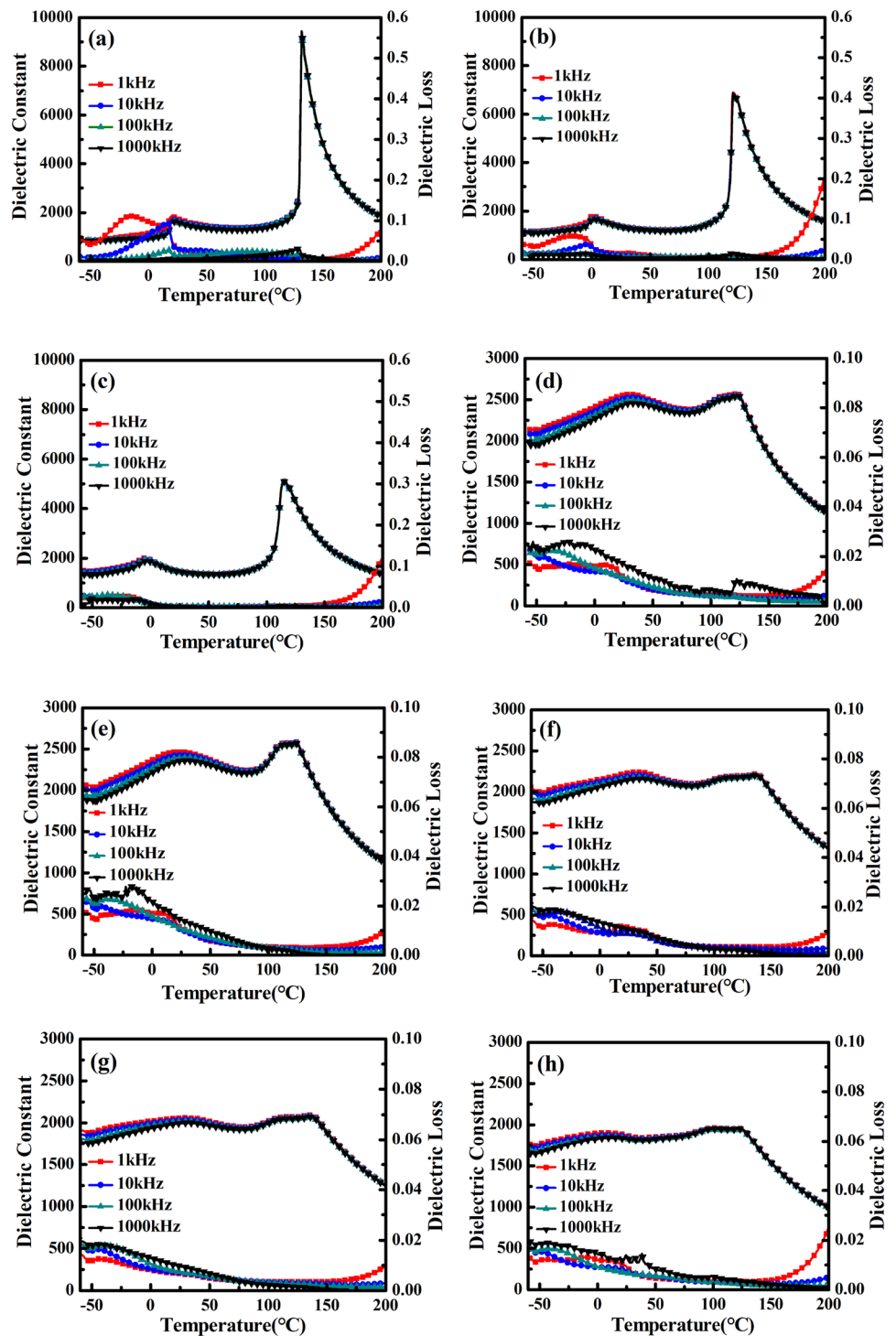
Fig. 6 The dielectric constant and dielectric loss as a function of temperature at 1–1000 kHz for BT@xMg ceramics **a** $x=0$, **b** $x=0.2$, **c** $x=0.4$, **d** $x=0.8$, **e** $x=1.0$, **f** $x=3.0$, **g** $x=5.0$, **h** $x=7.0$
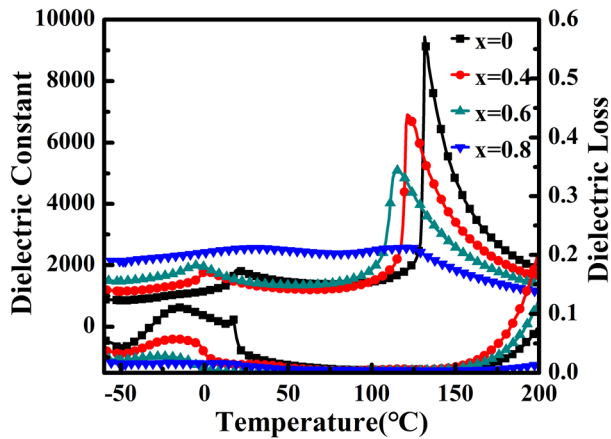
Fig. 7 The dielectric constant and dielectric loss as a function of temperature at 1 kHz for BT@xMg (x = 0–0.8 mol%) ceramics

Table 1 $\Delta C/C$ as a function of temperature, dielectric constant, and loss for different MgO contents at 1 kHz frequency

x	T_m (°C)	$\mathcal{E}_m$ (25 °C)	Tanδ (25 °C)	$\Delta C/C_{25\,°C} \leq \pm 15\%$
0	131.52	1733.19	0.031	–
0.4	121.16	1373.69	0.014	–
0.6	115,21	1455.56	0.002	–
0.8	123.06	2553.73	0.011	− 42.1 ~ 137.0
1	123.47	2461.62	0.011	− 40.7 ~ 140.0
3	136.71	2230.07	0.011	− 60.0 ~ 155.8
5	136.34	2057.21	0.007	− 60.0 ~ 158.8
7	123.19	1984.36	0.007	− 60.0 ~ 147.2

References

1. J.F. Scott, Science **315**, 954 (2007)
2. H. Hao, H. Liu, S. Zhang, B. Xiong, X. Shu, Z. Yao, M. Cao, Scr. Mater. **67**, 451 (2012)
3. S.-C. Jeon, C.-S. Lee, S.-J.L. Kang, E. Olevsky, J. Am. Ceram. Soc. **95**, 2435 (2012)
4. Y. Yuan, S.R. Zhang, X.H. Zhou, B. Tang, J. Mater. Sci. **44**, 3751 (2009)
5. H. Kishi, N. Kohzu, J. Sugino, H. Ohsato, Y. Iguchi, T. Okuda, J. Eur. Ceram. Soc. **19**, 1043 (1999)
6. C.-H. Kim, K.-J. Park, Y.-J. Yoon, M.-H. Hong, J.-O. Hong, K.-H. Hur, J. Eur. Ceram. Soc. **28**, 1213 (2008)
7. K.-J. Park, C.-H. Kim, Y.-J. Yoon, S.-M. Song, Y.-T. Kim, K.-H. Hur, J. Eur. Ceram. Soc. **29**, 1735 (2009)
8. Y.S. Jung, E.S. Na, U. Paik, J. Lee, J. Kim, Mater. Res. Bull. **37**, 1633 (2002)
9. L. Ben, D.C. Sinclair, Appl. Phys. Lett. **98**, 092907 (2011)
10. L. Zhang, O.P. Thakur, A. Feteira, G.M. Keith, A.G. Mould, D.C. Sinclair, A.R. West, Appl. Phys. Lett. **90**, 142914 (2007)
11. K. Madhan, R. Thiyagarajan, C. Jagadeeshwaran, A. Paul Blessington Selvadurai, V. Pazhanivelu, K. Aravinth, W. Yang, R. Murugaraj, J. Sol-Gel Sci. Technol. **88**, 584 (2018)
12. M. Liu, H. Hao, Y. Zhen, T. Wang, D. Zhou, H. Liu, M. Cao, Z. Yao, J. Eur. Ceram. Soc. **35**, 2303 (2015)
13. H. Gong, X. Wang, Q. Zhao, L. Li, J. Mater. Sci. **50**, 6898 (2015)
14. H. Miao, M. Dong, G. Tan, Y. Pu, J. Electroceram. **16**, 297 (2006)
15. L. Li, M. Wang, Y. Liu, J. Chen, N. Zhang, Ceram. Int. **40**, 1105 (2014)
16. J.S. Park, M.H. Yang, Y.H. Han, Mater. Chem. Phys. **104**, 261 (2007)
17. J.S. Park, Y.H. Han, Solid State Phenom. **124–126**, 811 (2007)
18. L. Xie, X. Huang, C. Wu, P. Jiang, J. Mater. Chem. **21**, 5897 (2011)
19. A. Kirianov, T. Hagiwara, H. Kishi, H. Ohsato, Jpn. J. Appl. Phys. **41**, 6934 (2002)
20. T. Nagai, K. Iijima, H.J. Hwang, M. Sando, T. Sekino, K. Niihara, J. Am. Ceram. Soc. **83**, 107 (2000)
21. J. Jeong, Y. Ho Han, Phys. Chem. Chem. Phys. **5**, 2264 (2003)
22. Y. Tsung Lin, S. Fu Ou, M. Horng Lin, Y. Ru Song, Ceram. Int. **44**, 3531 (2018)
23. J. Jeong, Y.H. Han, Jpn. J. Appl. Phys. **43**, 5373 (2004)
24. S.C. Tidrow, Ferroelectrics **470**, 13 (2014)
25. J. Pokorný, U.M. Pasha, L. Ben, O.P. Thakur, D.C. Sinclair, I.M. Reaney, J. Appl. Phys. **109**, 114110 (2011)
26. Y. Yang, H. Hao, L. Zhang, C. Chen, Z. Luo, Z. Liu, Z. Yao, M. Cao, H. Liu, Ceram. Int. **44**, 11109 (2018)
27. C.H. Perry, D.B. Hall, Phys. Rev. Lett. **15**, 700 (1965)
28. M.H. Frey, D.A. Payne, Phys Rev B **54**, 3158 (1996)
29. D. Lu, Y. Zheng, L. Yuan, Materials **12**, 10 (2019)
30. J.-H. Lee, S.-H. Yoon, D.-Y. Kim, J. Am. Ceram. Soc. **85**, 3111 (2004)
31. G. Zhang, D. Brannum, D. Dong, L. Tang, E. Allahyarov, S. Tang, K. Kodweis, J.-K. Lee, L. Zhu, Chem. Mater. **28**, 4646 (2016)